Title: **Mapping process model results to fracture model initial conditions for adhesive bonding**

Authors: Andrew C. Bergan[1]
Thammaia Sreekantamurthy[2]
James G. Ratcliffe[1]
Nelson V. De Carvalho[1]

PAPER DEADLINE: ****June 9, 2023****

PAPER LENGTH: ****6-16 PAGES** (Maximum – not counting cover page) **

Paper Number: **004558**

ABSTRACT

A systematic approach is proposed for mapping adhesive bonding process outcomes to initial conditions for progressive damage analysis (PDA). Herein, two mapping procedures are developed: 1) direct mapping for residual stresses, strains, and deformations obtained from a process model; and 2) functional mapping for quantities such as bondline thickness, degree of cure, and porosity that are assumed to have a functional relationship with fracture toughness but are not discretely modeled in the PDA. The spatial distribution of functionally mapped quantities may be determined by process modeling or inspection. The functional maps between the quantity of interest and fracture toughness may be obtained from independent lower-scale numerical simulations or empirical test campaigns. The proposed mapping procedure links the adhesive bonding process to the structural performance. Therefore, by accounting for the effects of bondline nonuniformities in structural analysis, analytical predictive accuracy can be improved, and off-nominal conditions can be evaluated. The mapping procedures are demonstrated and verified with example problems.

INTRODUCTION

Detailed progressive damage analysis (PDA) models for predicting damage and failure of composite structures typically rely on initial conditions representing a uniform idealized geometry and material state, e.g., [1, 2, 3]. In these models, material property inputs are intended to represent the initial material state information, including process details and deviations. One method to improve the predictive capability of PDA models is through a more realistic representation of the initial material state. Englestad et. al [4] described an approach to integrate computational cure process simulation, micromechanics, and fracture mechanics modeling, where residual stresses and strains from process model predictions serve as an initial state for PDA models. Larson et al.

[1] Durability, Damage Tolerance, and Reliability Branch, NASA Langley Research Center, Mail Stop 188E, Hampton, VA 23681

[2] Analytical Mechanics Associates, Hampton, VA 23681

[5] introduced manufacturing process-related effects as initial conditions for PDA in the context of adhesive bonded joints by including the stochastic nature of cure process defects in the damage analysis. In this paper, an approach is developed to spatially map manufacturing process results to PDA model initial conditions for secondary adhesive bonding applications. This approach offers the opportunity to link manufacturing process parameters to structural performance.

In secondary adhesive bonding, there are several sources of nonuniform initial conditions, e.g., bondline thickness, surface preparation, porosity, degree of cure, and residual stresses, referred to herein as manufacturing quantities of interest (MQOI). The MQOI influence the structural strength and damage tolerance. Moreover, variations in such quantities across structures are often unavoidable due to factors such as geometry, layup, tooling, and cure cycle. Therefore, it is highly desirable to include these factors and their distributions in predictions of strength and damage tolerance.

The MQOI can be predicted as continuous field variables by manufacturing process models. In some cases (e.g., bondline thickness), they can also be readily measured by nondestructive inspection (NDI). Given known MQOI, the task pursued in this paper is introduction of this data as initial conditions in a PDA model. The PDA model used to represent bondline fracture is assumed to have a cohesive element layer to model bondline fracture in the cohesive mode (i.e., at the mid-plane of the bondline). The loading is restricted herein to mode I conditions. However, the mapping framework is intended to be extensible to more sophisticated PDA models for consideration of different loading conditions and inclusion of additional failure modes.

The remainder of this paper is organized as follows. First, the mapping framework is described, which includes two mapping approaches: direct and functional. Then, the following two sections elaborate on the direct and functional mapping approaches, respectively. The mapping procedures and some implementation details are described. Numerical exercises are presented and discussed for verification and demonstration.

MAPPING FRAMEWORK

In this paper, a framework is developed comprising two methods for mapping manufacturing process results to PDA model initial conditions: direct and functional, as shown schematically in Figure 1. These mapping approaches apply to a single MQOI but are formulated such that they may be used in concert to represent the combined effect of several MQOI. As will be described, the mapping procedures are a set of interpolations from a manufacturing result (source) to a PDA model (target) using scripts and subroutines in Abaqus[†].

In direct mapping (Figure 1a), the MQOI, Q_i, has a corresponding analytical representation in both the process model $Q_i(\boldsymbol{x})$ and PDA model $Q_i(\tilde{\boldsymbol{x}})$ where the tilde indicates the coordinates may differ between the two models. Direct mapping is used herein for residual stresses, strains, and displacements for the adhesive and adherends.

In functional mapping (Figure 1b), Q_i is assumed to be a scalar quantity describing the adhesive that has a known functional relationship to fracture toughness, $\bar{G}_c =$

[†] Specific vendor and manufacturer names are explicitly mentioned only to accurately describe the software, material, or test hardware. The use of vendor and manufacturer names does not imply an endorsement by the National Aeronautics and Space Administration (NASA) nor does it imply that the specified material or equipment is the best available.

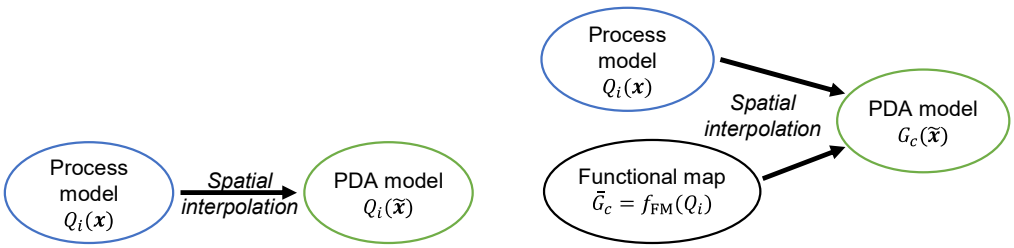

Figure 1. Two mapping approaches developed herein. Example quantities $Q_i(\boldsymbol{x})$ for direct mapping are residual strains, stresses, and deformation, which herein are treated by equivalent nonmechanical strains. Example quantities $Q_i(\boldsymbol{x})$ for functional mapping are bondline thickness, porosity, and degree of cure.

$f_{\mathrm{FM}}(Q_i)$. Given f_{FM} and the process model result $Q_i(\boldsymbol{x})$, the fracture toughness is prescribed in the PDA model $G_c(\tilde{\boldsymbol{x}})$. Functional mapping is used herein for bondline thickness. It may also be applied to porosity (see [6, 7] for numerical simulations that provide a basis for f_{FM}) and degree of cure. The details for direct mapping are described next, followed by functional mapping.

DIRECT MAPPING

Direct mapping applies when the process model and PDA model share the same representation of the MQOI. For adhesive bonding, process-induced residual stresses, strains, and deformations are handled by the direct mapping approach. The approach adopted is to interpolate the equivalent nonmechanical strain, $\varepsilon_{\mathrm{eqnms}}$, between the two meshes as proposed previously [4, 8, 9]. The formulation, implementation, and a numerical example are described in the remainder of this section.

Formulation

The equivalent nonmechanical strain is the stress-free strain resulting from the cure process, calculated as

$$\varepsilon_{\mathrm{eqnms}} = \varepsilon_{\mathrm{cure}} - C^{-1}\sigma_{\mathrm{cure}} \tag{1}$$

where $\varepsilon_{\mathrm{cure}}$ and σ_{cure} are the total strains and residual stresses at the end of the cure process and C is the stiffness tensor for the cured material. $\varepsilon_{\mathrm{eqnms}}$ is an analog to the thermal strain and the two are equivalent when the cure process is modeled as a linear thermal cooldown ($\alpha\Delta T$). In the subsequent PDA model, $\varepsilon_{\mathrm{eqnms}}$ is taken as the initial free strain. During an initial step, prior to applying mechanical load, the residual stresses, strains, and deformations are recovered by satisfying equilibrium. Stress in the PDA is calculated as

$$\sigma = C\left(\varepsilon - \varepsilon_{eqnms}\right). \tag{2}$$

Since the residual stress in the PDA is recovered by equilibrium, differences in the mesh between the two models leads to differences in the residual stress fields. However, the approach guarantees the residual stress is approximated to the extent possible by the PDA model mesh while satisfying equilibrium.

Implementation

The direct mapping approach is implemented in using a set of Python scripts and user subroutines as follows. Assume that the $\varepsilon_{\text{eqnms}}$ are calculated from process model results using (1) at the integration point locations. The implementation tasks are to 1) interpolate $\varepsilon_{\text{eqnms}}$ at the PDA model integration point locations and 2) initialize $\varepsilon_{\text{eqnms}}$ as an initial free strain.

The interpolation of $\varepsilon_{\text{eqnms}}$ from the process model to the PDA model is implemented assuming the two models have dissimilar meshes following the algorithm proposed by Mayer et al. [10] and briefly summarized here. For each integration point in the PDA model (target) mesh, the algorithm searches to find the enclosing element in the process model (source) mesh and uses that element's shape function to interpolate $\varepsilon_{\text{eqnms}}$. The search is performed using a three-dimensional (3D) global bucket sort [11]. The bucket sort accelerates the search by limiting the search domain for each target integration point. The target integration points and source mesh nodes are grouped into a regular orthogonal grid of buckets by their coordinates. The bucket size is a user defined parameter. For each target integration point, the search for the enclosing element is performed with the domain reduced to a set of candidate elements identified as those connected to nodes that lie within the bucket. A two-dimensional (2D) example is shown in Figure 2, where the gray 'x' symbols are the PDA model (target) integration points that lie within the current bucket with boundary shown by blue dashed lines. The candidate elements of the process model (source) mesh are shown with solid lines and numbered 1 to 6. Considering the bold 'x' as the current target integration point, $\boldsymbol{p}$, the candidate elements are sorted by the distance to the element centroid $\|\boldsymbol{p} - \boldsymbol{e_c}\|$ where $\boldsymbol{e_c}$ is the element centroid (1, 2, 4, 5, 3, 6 in Figure 2). For each candidate element in the source mesh, the natural coordinates (ξ, η, μ) of the target integration point are calculated by Newton-Raphson iterations and the enclosing element is identified when $-1 \leq \xi, \eta, \mu \leq 1$. In the case shown in Figure 2, element number 4 is the enclosing element. Knowing the enclosing element and ξ, η, μ for the target integration point location, $\varepsilon_{\text{eqnms}}$ is interpolated using the shape functions. The process is repeated for each integration point in the PDA model mesh and the results are written to a file. The $\varepsilon_{\text{eqnms}}$ file is read into Abaqus with the user subroutine SDVINI and initialized as state variables 1 through 6. Then, the data are initialized as a free strain in the model by the

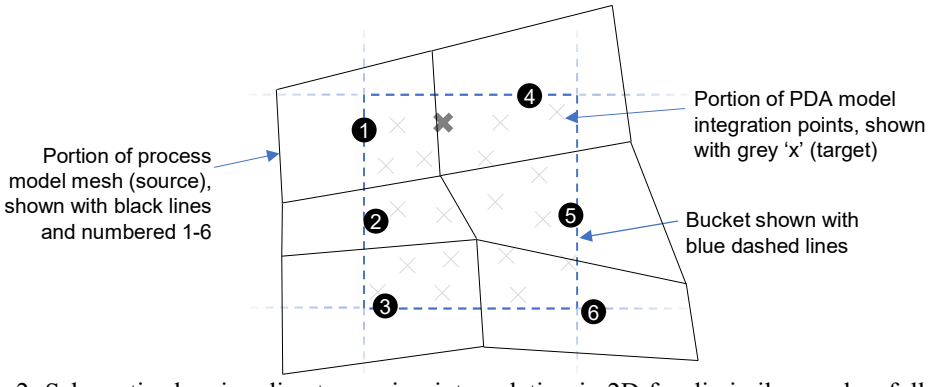

Figure 2. Schematic showing direct mapping interpolation in 2D for dissimilar meshes following the bucket sort algorithm proposed by Mayer et al. [10]. The bold 'x' is identified as enclosed by element 4 by its natural coordinates, based on which it is trivial to interpolate $\varepsilon_{\text{eqnms}}$ at the location of 'x'. The concept extends naturally to 3D.

analogy to thermal strain. In the user subroutine UEXPAN, $\varepsilon_{\text{eqnms}}$ are defined as increments in thermal strain and $\Delta T = 1$ is applied. Depending on the process model, $\varepsilon_{\text{eqnms}}$ may have nonzero coupling terms. Therefore, the `type = anisotropic` option is used so that all six components of $\varepsilon_{\text{eqnms}}$ are included.

Example: Residual stresses in a double cantilever beam specimen

A specific double cantilever beam (DCB) specimen configuration with residual thermal stresses is considered as a numerical exercise to demonstrate the direct mapping procedure. The specimen is modeled in Abaqus with two parts corresponding to the two relatively thick arms, as shown in Figure 3a. The specimen layup is [90/0_n/90], where the pre-crack is located at the midplane of the central 0-degree ply block. As such, the arms are unsymmetric. The width of the specimen, which is 2 mm, is discretized with a single row of elements. The configuration is strictly a numerical exercise but is perhaps relevant to a co-cured configuration. Dissimilar meshes are considered for the process model and structural model (Figure 3b) with the overlay highlighting the lack of consistency in the two meshes besides the fact that the material boundary (0/90) is held consistent. The models use 3D continuum solid elements with incompatible modes (Abaqus type C3D8I). Since the process model results were not available, a pseudo process model is used for demonstration purposes where residual stresses are calculated by a thermal cooldown step with $\alpha\Delta T$. Elastic constants and coefficients of thermal expansion for IM7-8552 are used from Wanthal et al. [12]. The exercise is limited to recovering the residual stresses, strains, and deformation and so the target model is a simple structural/stress model without PDA features. A logical next step is to include a

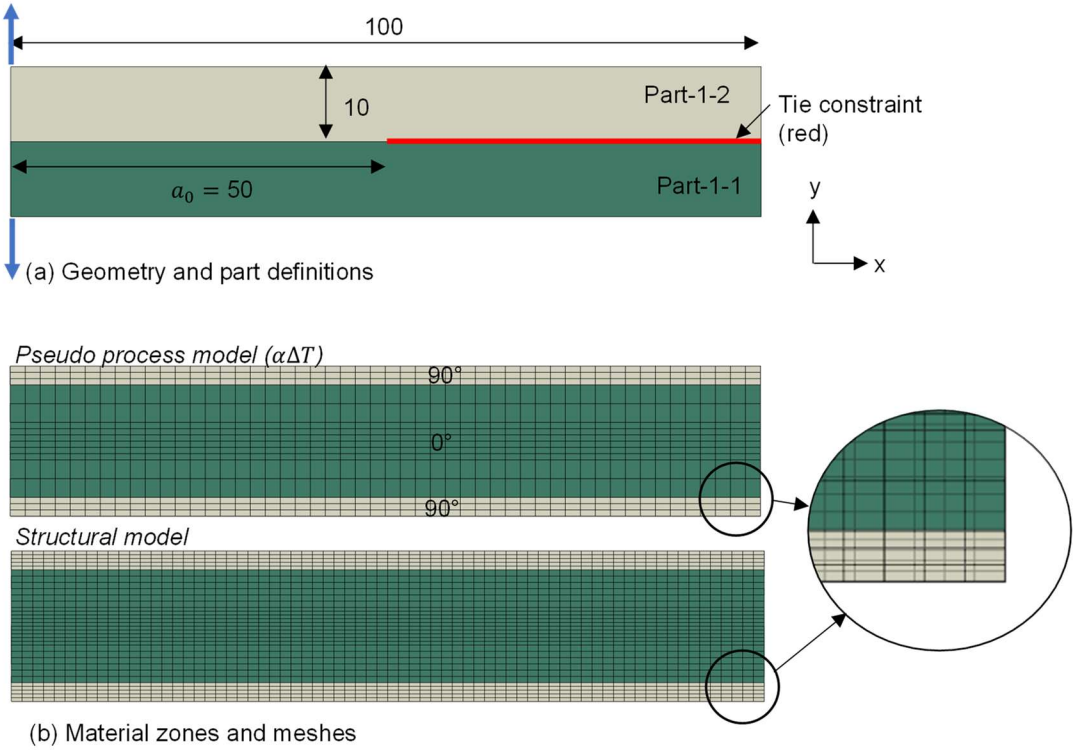

Figure 3. Geometry and mesh for the direct mapping example. The dimensions are in mm.

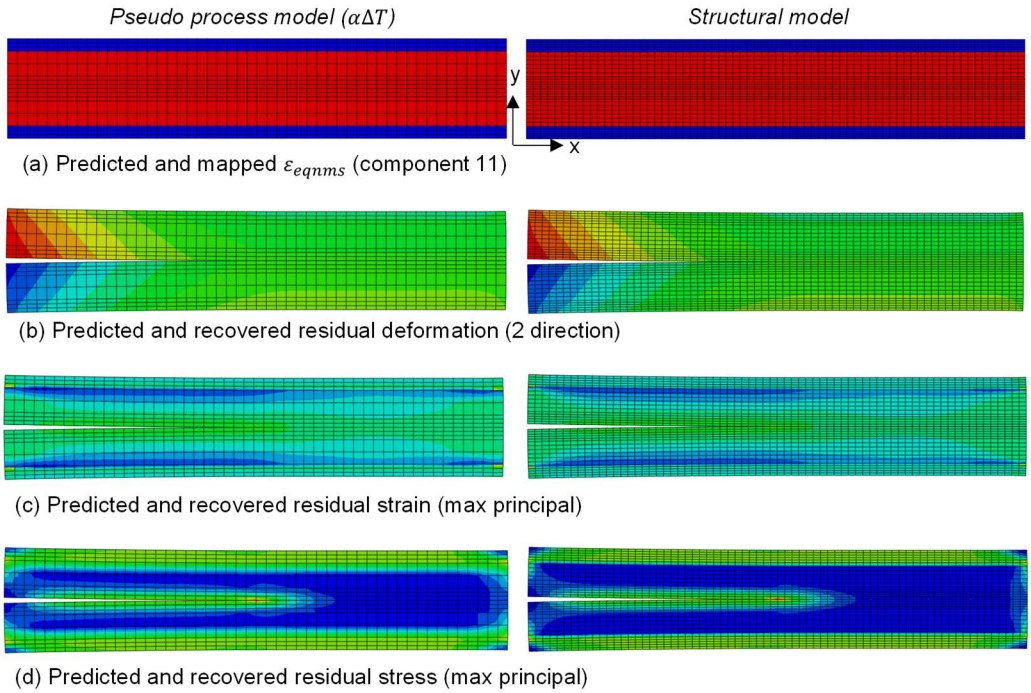

Figure 4. Direct mapping example with uniform ΔT.

cohesive element layer to evaluate the influence of the residual stresses on the damage propagation behavior.

First, consider the case where a uniform ΔT is applied in the pseudo process model. The results from the process model are shown in the left column of Figure 4. The $\varepsilon_{\mathrm{eqnms}}$ calculated as $\alpha\Delta T$ are a function of the layup and the unsymmetric layup produces an opening in the pre-crack region. The results from the structural model after the mapping procedure and equilibrium step are applied are shown in the right column of Figure 4. The fields correspond nearly exactly with only minor differences due to the differences in the two meshes (for example near the ply interface).

Next, to verify the procedure for a more complex $\varepsilon_{\mathrm{eqnms}}$ field, an arbitrary nonuniform ΔT shown in Figure 5 is prescribed in the pseudo process model. The results from the process model for the three direct components of $\varepsilon_{\mathrm{eqnms}}$ are shown in the left column of Figure 6. The results after the direct mapping procedure are shown in the right column of Figure 6. Very similar fields are observed with only minor differences noted near the ply interfaces where large gradients are present. Similar to the case shown in Figure 4, the residual stresses, strains, and deformations are recovered after finding equilibrium and comparing back to the pseudo process model results show only minor differences related to the dissimilar meshes.

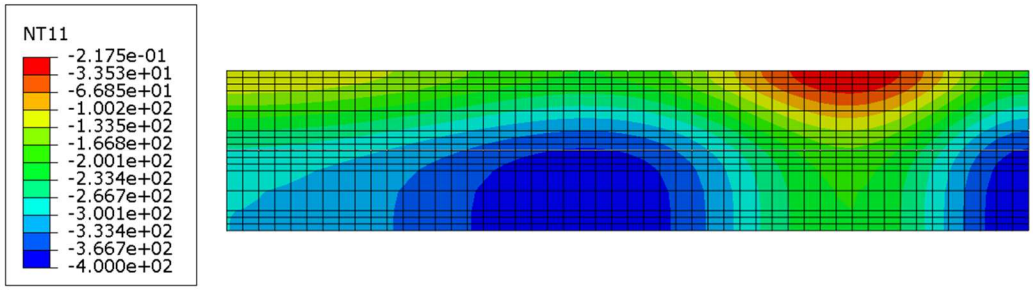

Figure 5. Nonuniform ΔT field.

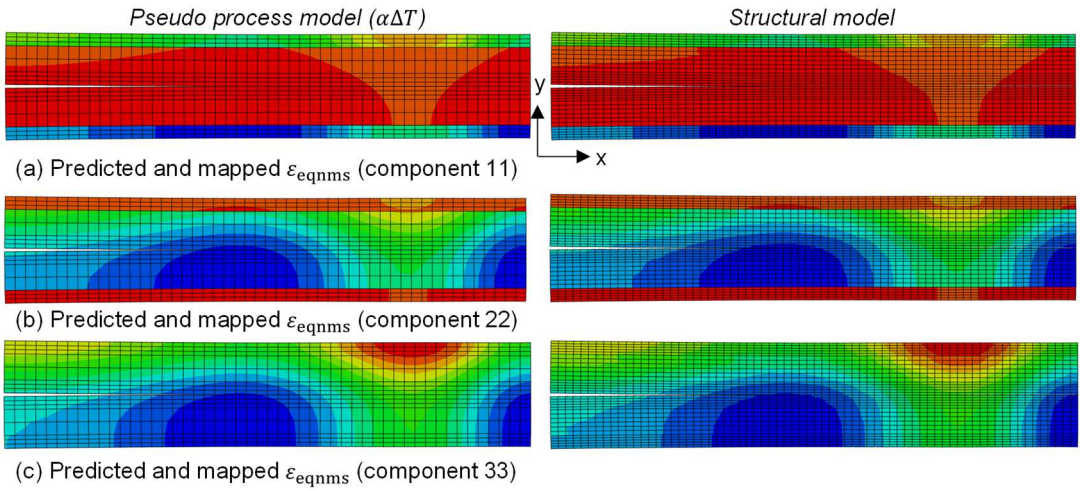

Figure 6. Direct mapping example with nonuniform ΔT.

FUNCTIONAL MAPPING

Functional mapping is used for MQOI that influence fracture toughness, but through a mechanism that cannot be easily introduced into the PDA model. The MQOI considered herein for functional mapping is bondline thickness. It has been shown that fracture toughness varies with bondline thickness with an important mechanism being development of the plastic zone in the adhesive layer [13, 14]. When the plastic zone is constrained in relatively thin bondlines, energy dissipation is reduced due to the smaller plastic zone. This phenomenon can be modeled, but several elements are required through the thickness of the adhesive layer to obtain a converged solution [14], which is intractable for many problems, and the material characterization is challenging.

The functional mapping approach abstracts the mechanisms that relate the MQOI to fracture toughness into a functional relationship that can be characterized empirically or numerically. The formulation, implementation, and numerical examples are described in the remainder of this section.

Procedure

The functional mapping routine comprises three steps for each integration point in the PDA model cohesive layer representing fracture in the adhesive. First, linear interpolation is used to find the thickness, t (i.e., MQOI value). Linear interpolation is selected for its simplicity and applicability to different data sources such as process model results and NDI results. The next step is application of the functional map, f_{FM}, to compute the fracture toughness corresponding to the thickness t. The functional map returns normalized fracture toughness $\bar{G}_c = G_{c,t}/G_c$ where $G_{c,t}$ is the toughness associated with the current thickness and G_c is the nominal fracture toughness for a standard thickness. $\bar{G}_c$ is therefore a scale factor that can be multiplicatively combined with scale factors mapped from other MQOI, e.g., porosity. Finally, the traction separation law is scaled by $\bar{G}_c$. It is assumed that the shape of TSL remains constant at all locations. The process is shown schematically in Figure 7.

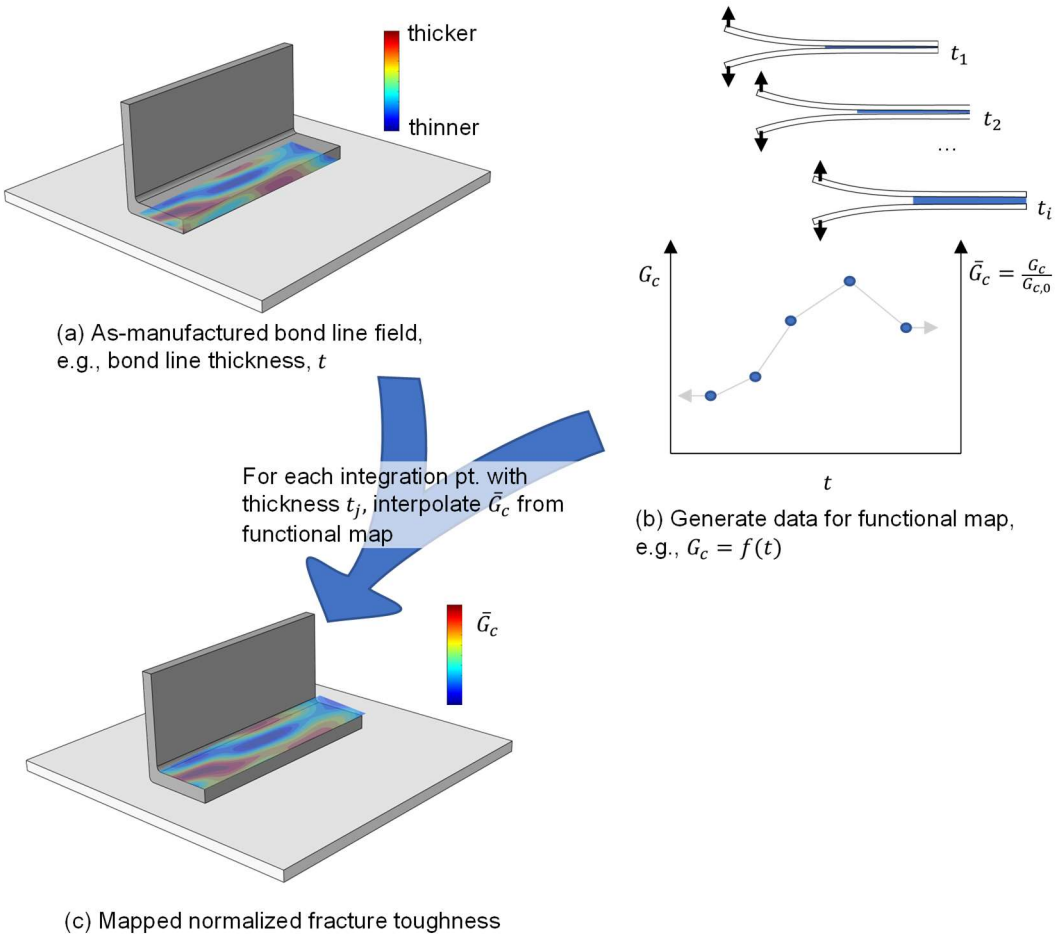

Figure 7. Schematic illustration of the functional mapping procedure.

Implementation

The functional mapping routine is implemented in Abaqus through a series of Python scripts and user subroutines as follows. The first step of the procedure, spatial interpolation of thickness is implemented in Python using LinearNDInterpolator, a multidimensional piecewise linear interpolator, available in the SciPy package [15]. The remaining steps are implemented using the Abaqus user subroutines SDVINI and UMAT. The thickness data are read into Abaqus and initialized as a state variable for visualization using SDVINI. A UMAT is used for the cohesive element constitutive model. The cohesive element constitutive model implemented in the UMAT is the piecewise-linear generalizable cohesive element (PLIGCOE) [16]. In the PLIGCOE, the traction-separation laws (TSLs) are defined by m points, $\boldsymbol{p}$, corresponding to a change in slope, $S = \{\boldsymbol{p}_1, \dots, \boldsymbol{p}_m\}$ where $\boldsymbol{p}_1 = (\delta^{p_1}, \sigma^{p_1})$.

The functional map f_{FM} is implemented as a piecewise linear curve. For values below the minimum thickness and above the maximum thickness, extrapolation with a constant value is assumed. The $\bar{G}_c$ is obtained from f_{FM} and used to modify the TSL definition to $\hat{S} = \{\hat{\boldsymbol{p}}_i\}, i = 1 \dots m$ where $\hat{\boldsymbol{p}}_i = \left(\delta^{p_i}\sqrt{\bar{G}_c}, \sigma^{p_i}\sqrt{\bar{G}_c}\right)$. The remainder of the PLIGCOE constitutive model proceeds as described in [16] with $\hat{S}$ in place of S.

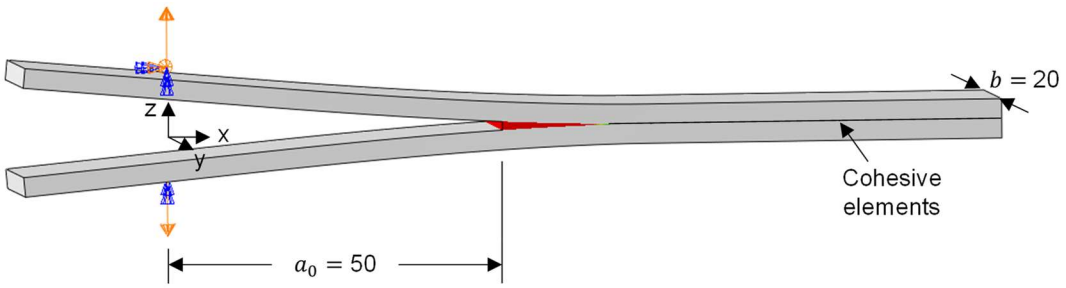

(a) Model configuration

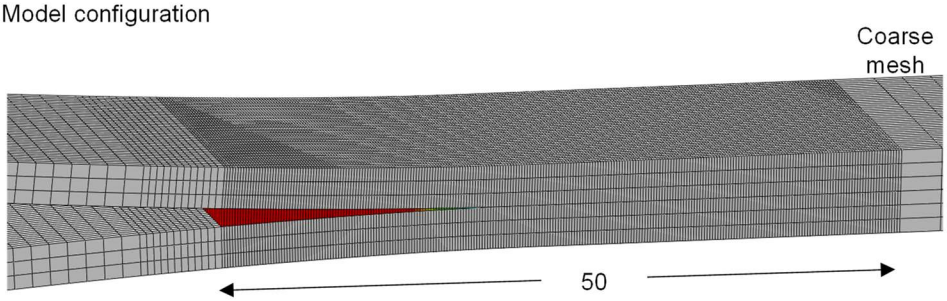

(b) Mesh refinement near the crack tip

Figure 8. Model configuration used for the functional mapping examples. The dimensions are in mm.

Example: Bondline thickness in an adhesively bonded DCB specimen

Numerical exercises are provided for functional mapping of bondline thickness in an adhesively bonded DCB specimen to demonstrate the capability of the functional mapping routine. The DCB specimen adherends are 3-mm-thick unidirectional laminates modeled with three C3D8I elements through the thickness using IM7/8552 material properties [12]. The model configuration and mesh are shown in Figure 8. A zero-thickness cohesive element layer represents the adhesive at the interface between the adherends. The typical element size is 0.2 mm in the crack propagation region. The functional mapping is applied and the simulations are run using a static step in Abaqus [17]. Three cases are included as follows. The first case considers a one-dimensional (1D) thickness variation with synthetic thickness and functional map to allow for verification that the correct propagation toughness is recovered. The second case also considers a 1D thickness variation but uses data from a process model along with experimental measurements. The third case considers a 2D thickness variation to demonstrate the capability and show how the functional mapping can manifest in crack front propagation behavior.

1D BONDLINE THICKNESS VARIATION – VERIFICATION

The DCB specimen described above is analyzed with uniform bondline thickness and with a synthetic longitudinal variation in bondline thickness to verify the functional mapping implementation. In both cases, the analysis results are used to calculate the fracture toughness by the J-integral method where $J = 2P\theta/b$, where P is the load and θ the arm rotation at the load application point [18]. The objective of this verification exercise is to recover the input fracture toughness. The models use a cohesive layer with an arbitrary trilinear TSL with strength $\sigma = 51$ MPa, nominal toughness $G_{c,0} =$

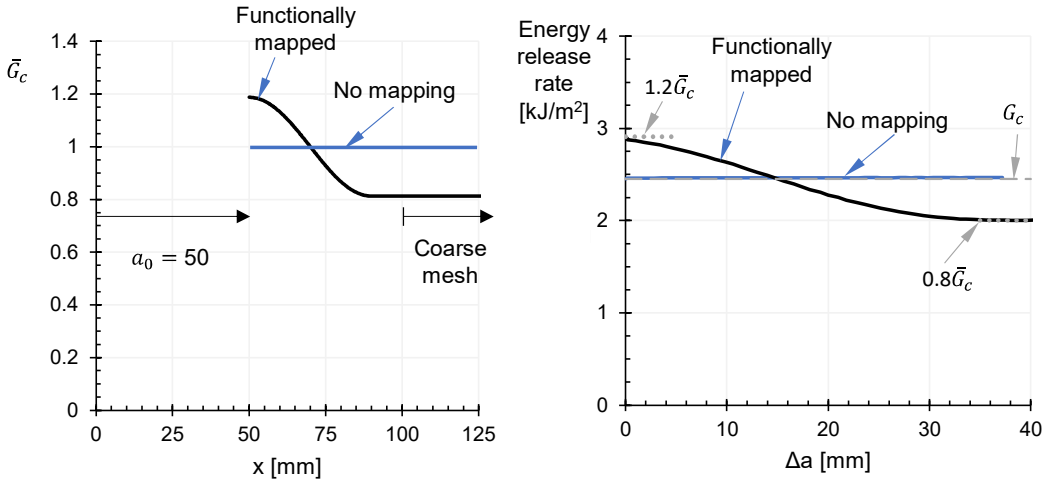

(a) Prescribed $\bar{G}_c$ resulting from a sinusoidal thickness vs. position and linear f_{FM}

(b) Predicted R-curve obtained from numerical computation of the J-integral as a function of crack extension, Δa

Figure 9. 1D functional map verification exercise showing that the DCB model reproduces the input fracture toughness. The blue lines show the case where the functional map is disabled. The gray lines in (b) show the input toughnesses for reference.

2.45 kJ/m^2, and a critical separation of 0.24 mm at which point the traction is zero. The initial conditions for $\bar{G}_c$ as a function of position are shown in Figure 9a, obtained from a thickness variation and functional map selected for illustrative purposes as follows. The 1D variation case starts with a thick bondline such that the toughness is 20% above $G_{c,0}$ (2.9 kJ/m^2) at the initial crack front and then the thickness decreases sinusoidally to the point where the toughness is 20% below $G_{c,0}$ (2.0 kJ/m^2) over 50 mm < x < 90 mm, after which thickness and therefore toughness remain constant. The results are shown in Figure 9b where it is observed that the fracture toughness calculated from the J-integral reproduces the input in that a sinusoidal variation in the R-curve is predicted starting 20% above $G_{c,0}$ and reaching a plateau 20% below $G_{c,0}$. The results are contrasted against the case where the functional mapping is disabled (blue curves).

1D BONDLINE THICKNESS VARIATION – DEMONSTRATION

Next, a similar case is considered but with bondline thickness data obtained from a process model result and the functional map obtained from test measurements. This demonstration serves to illustrate the importance of the functional mapping approach in adhesive fracture evaluation for the FM 209-1U† unsupported film adhesive [19]. First, the process model and its predicted bondline thickness variation are described. Then, a set of tests used to generate a functional map for bondline thickness are summarized. Finally, results generated with the functional mapping approach are presented and discussed.

A process model is being developed for adhesive bonding simulations of composite laminates. The objective is to use such models to predict bondline characteristics and cure defects that will serve as an initial condition for PDA models. The process model considers autoclave bonding of two 12-inch square cured laminates with a film adhesive and a Teflon insert to produce DCB specimens. The simulation is conducted using COMPRO† [9] and Abaqus [20] and accounts for heat transfer, fiber-bed compaction,

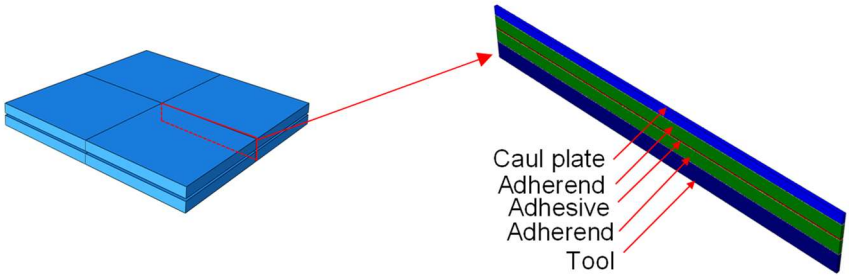

Figure 10. Process model configuration showing the thin-strip plane strain modeling approach with a symmetry plane at the center of the panel and the entities included in the model.

resin bleed, cure shrinkage, and thermal expansion and contraction effects in the material using 3D continuum finite elements. The model includes discrete representation of the adhesive material layer, composite adherends, caul, and tool plate. The cure process simulation is performed using three sequential modules of COMPRO, each performing a distinct analysis function: 1) thermo-chemical (includes heat transfer and cure-kinetics), 2) flow-compaction, and 3) thermo-mechanical (stress analysis). The flow-compaction analysis includes the resin bleed and fiber-bed compaction to predict fiber volume fraction distribution in the consolidated part (i.e., if the adhesive has a fibrous carrier), and to predict the thickness of the adhesive layer. The stress-deformation simulation is based on the thermal response of the part and tool assembly, and the fiber volume fraction distribution computed from the previous analyses. The tool-removal step is included as a model change. The stress-deformation results include residual stresses, strains, and deformations after tool removal.

At the present time, the process model is under development, and so some simplifying assumptions are used, and model validation is future work. Nonetheless, the process model provides representative results for functional mapping. The FM209-1U adhesive material characterization and validation is in progress, and so input properties are assumed based on available data and engineering judgement. The model includes several elements through the thickness of the bondline to capture the physics of resin flow and compaction. The bondline is quite thin and therefore dictates relatively small element sizes to maintain acceptable aspect ratios. To minimize the computational expense, the model uses a thin strip with a plane strain idealization, as shown in Figure 10. Bondline thickness data are extracted using a post processing script.

A set of fracture toughness characterization tests were conducted on specimens obtained from three different panels with different bondline thicknesses to generate a bondline thickness functional map. The panels were prepared by secondary bonding of cured unidirectional 26-ply IM7/8552 panels with FM209-1U adhesive in an autoclave. A Teflon film was included near the midplane covering a portion of the bonded surface to form the initial debond. The bonded panels differed only by the number of layers of adhesive used for bonding, which were 1, 2, and 4, designated herein as panels P1, P2, and P4, respectively. The adhesive was cured by applying vacuum, then adding 25 psi pressure, ramping to 121°C at 1.7°C/min, holding for 90 minutes, cooling down, and releasing pressure. After the cure cycle, representative bondline thickness measurements were made using optical microscopy. The bondline thicknesses were 0.122 mm, 0.231 mm, and 0.467 mm for panels P1, P2, and P4, respectively.

Mode-I interfacial fracture toughness was measured following procedures described in ASTM D5528 [21] for three specimens of each configuration. The DCB test

geometry was utilized with a 55.9-mm-long initial debond and a 20-mm width. Load was introduced via a 3.8 mm-diameter hole drilled at the mid-plane across the specimen width. Twelve-megapixel cameras were positioned on both sides of the specimen to enable documentation of debond growth during testing, which was highlighted by white matte enamel paint applied to both specimen edges. The tests were conducted in a servo-hydraulic load frame using a force indicator with a ±1330-N full scale and a crosshead displacement indicator with a ±76-mm full scale. Load was applied under stroke control at a rate of 1 mm/min. The specimens were unloaded at the same rate after a nominal 5 mm of debond growth and then reloaded until the debond grew nominally 50 mm so that non-pre-cracked and pre-cracked toughness could be measured. Load and crosshead displacement data were recorded during the entirety of a test at 10 Hz, while images were recorded at 0.5 Hz.

The test specimens from P1 and P2 exhibited mostly smooth and stable fracture propagation in a cohesive failure mode. In contrast, the test specimens from P4 had large unstable fracture propagation and significant regions of adhesive failure. Thus, the focus here is limited to P1 and P2. The average pre-cracked fracture toughness results obtained from the maximum load and compliance calibration are 1.67 kJ/m^2 and 2.61 kJ/m^2 for P1 and P2, respectively. The coefficients of variation for the data from panels P1 and P2 are 4.9% and 4.6%. The non-pre-cracked and pre-cracked toughness values differed by less than 5%. The R-curves show a slight decrease in toughness with propagation, which is not completely understood at this time. The fracture surfaces are shown in Figure 11 with the light gray color on both specimen halves indicative of stable cohesive fracture over the majority of the fracture surfaces. The dark gray regions on the right ends and in specimen P2-12 are regions where the crack propagated rapidly. In specimen P2-12 some adhesive fracture is noted in the vicinity of the rapid crack propagation. In all specimens, porosity is observed by small black circles mirrored on the two specimen halves (worst in specimen P1-01). Finally, the edges of the specimens exhibit some adherend delamination that appears to develop in the first few millimeters ahead of the insert (observed as black strips along specimen edges), which apparently results from the local 3D stress state near the free edge.

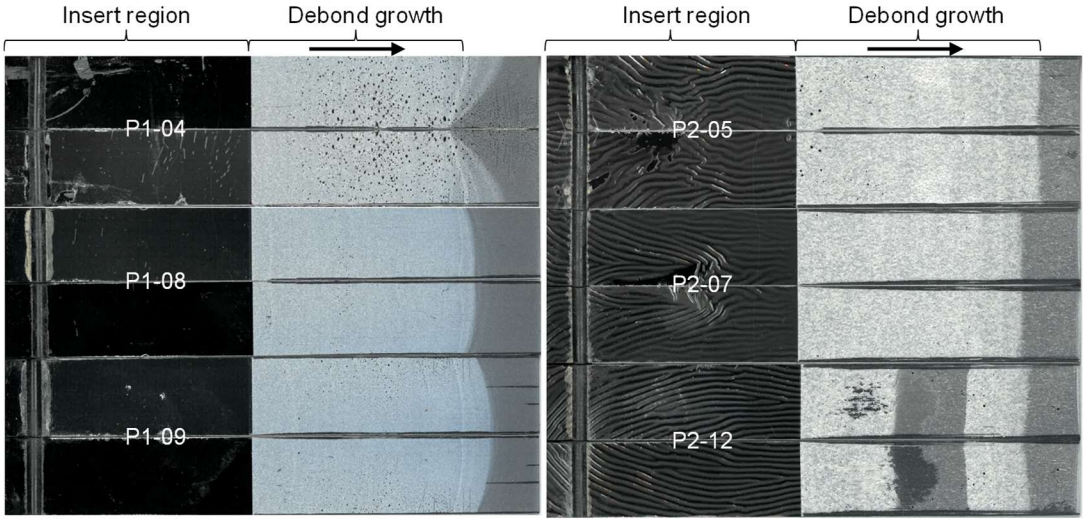

Figure 11. Fracture surfaces of specimens used to generate bondline thickness functional map.

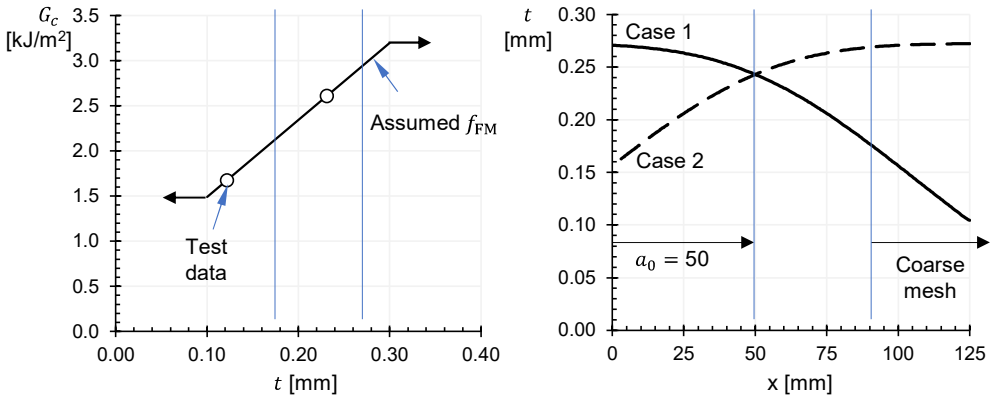

(a) Linear f_{FM} based on test data

(b) Thickness variation

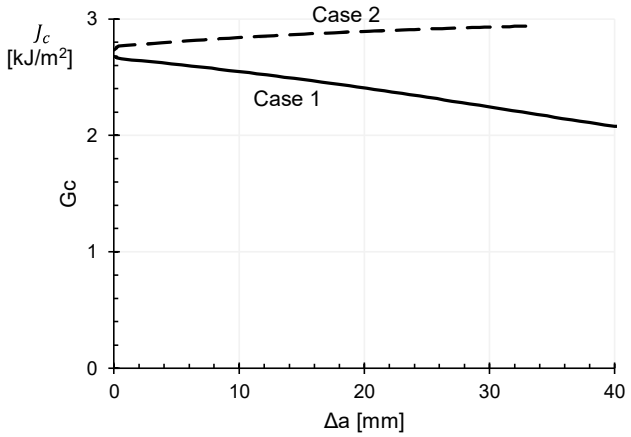

(c) Predicted R-curve obtained from numerical computation of the J-integral as a function of crack extension, Δa

Figure 12. Functional map and spatial variation in thickness obtained from test and process modeling, respectively, along with the predicted R-curve. In b and c, the solid and dashed curves correspond to load application near the panel center and near the panel edge, respectively.

The test results from P1 and P2 and the process model results form the inputs for the functional mapping procedure. The functional map, f_{FM}, is assumed linear through the range of bondline thicknesses in consideration, as shown in Figure 12a, since only two data points are available. The spatial variation in bondline thickness obtained from the process model results is shown with the solid curve in Figure 12b (case 1) where the insert and load application point are located near the center of the panel and the crack grows toward the free edge of the panel into adhesive with decreasing thickness. A second case is also considered, shown with the dashed curve in Figure 12b (cases 2), where the insert and load application are located on the opposite end (near the panel edge) so that the crack propagates into adhesive with increasing thickness. In the two cases, the bondline thickness at the insert edge is nearly the same. The range of thicknesses included in the crack propagation region of the DCB are shown with the blue vertical lines in Figure 12a and b. The predicted R-curves are shown in Figure 12c. The results show that a relatively small variation in bondline thickness has a substantial effect on the DCB test results. Not only does the toughness vary by up to 20% through crack propagation due to the bondline thickness variation, but the location of the Teflon insert on the panel determines whether a rising R-curve or falling R-curve is observed.

2D BONDLINE THICKNESS VARIATION

As a final example, a 2D thickness variation is considered using the same DCB model shown in Figure 8. As in the first functional mapping example, synthetic input data is used. In this case, the input data is constructed such that the crack front shape changes as the crack propagates from an inverted thumbnail shape due to high toughness at the center of the specimen to the conventional thumbnail shape at some distance from the insert where the toughness is uniform across the width. The functional map, bondline thickness field, and resulting $\bar{G}_c$ field are shown in Figure 13. The $\bar{G}_c$ field varies in x and y just ahead of the initial crack front. At about 30 mm ahead of the initial crack front, $\nabla\bar{G}_c = 0$. The input values are selected such that the effect of $d\bar{G}_c/dy \gg dG/dy$ at the initial crack front where G is the strain energy release rate and dG/dy is due to anticlastic bending. As a result, the thickness variation is critical to the shape of the crack front. As the crack propagates, at some point $d\bar{G}_c/dy \ll dG/dy$ and so

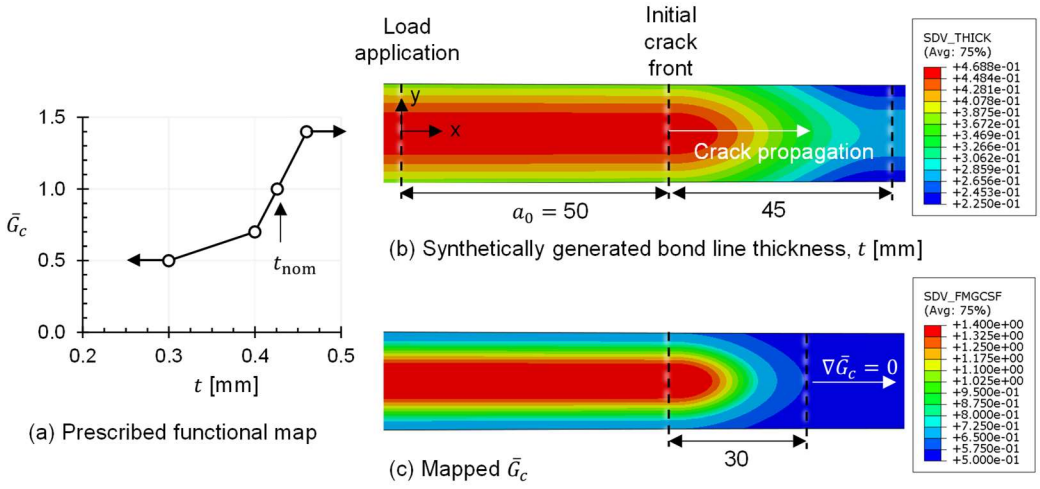

Figure 13. Initial conditions used for demonstrating functional mapping with a 2D variation in bondline thickness. The dimensions are in mm.

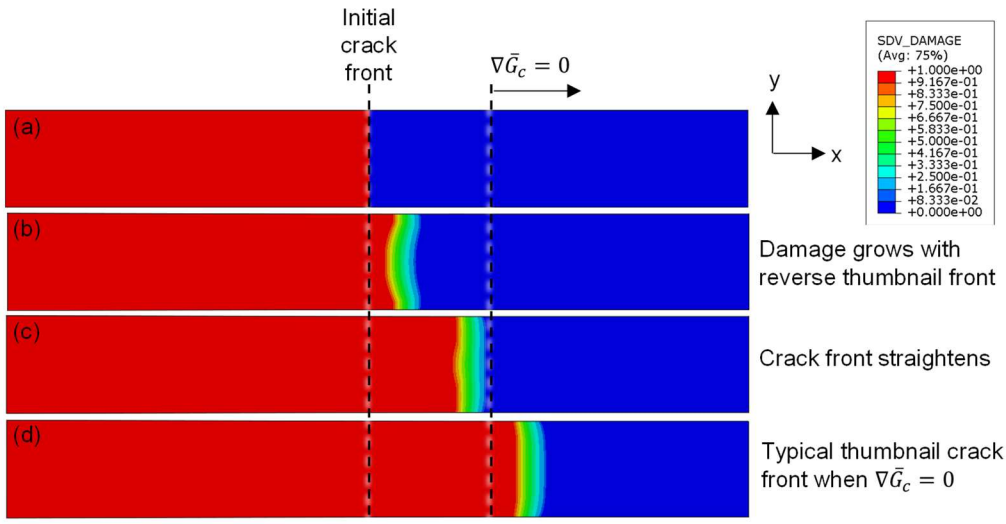

Figure 14. Damage variable contour plots showing crack propagation at several points in the load history. The functional mapping produces a transition from an inverted to conventional thumbnail shaped crack front as a result of the assumed inputs shown in Figure 13.

anticlastic bending drives the shape of the crack front. This behavior is successfully reproduced by the model, as shown in Figure 14.

SUMMARY

In secondary adhesive bonding, parameters including bondline thickness, porosity, and residual stresses are outcomes of the manufacturing process and often vary spatially throughout the bonded joint due to factors such as geometry, layup, tooling, and cure cycle. These parameters influence the structural strength and damage tolerance and thus are desirable to include in PDA models, but often are not considered. Therefore, the aim of this paper is to address this gap by introducing a systematic framework to include process results as initial conditions in PDA models and establish a numerical link between the adhesive bonding process and resulting structural performance.

The developed framework includes direct mapping for residual stresses, strains, and deformations and functional mapping for quantities such as bondline thickness, degree of cure, and porosity that are assumed to have a functional relationship with fracture toughness but are not discretely modeled in the PDA. Direct mapping is accomplished by interpolating the equivalent nonmechanical strain, $\varepsilon_{\mathrm{eqnms}}$, between the process model and PDA model. The interpolation is carried out using the process model mesh and shape functions with a computationally efficient search algorithm. Functional mapping is used for quantities that influence fracture toughness, but through a mechanism that cannot be easily introduced into the PDA model. The functional mapping implementation is generalizable, but bondline thickness is the focus of this paper. The functional mapping is carried out using linear interpolation based on 1) a functional map between the bondline thickness and fracture toughness, and 2) a bondline thickness field.

Numerical exercises are used to verify and illustrate the capability. In most cases, synthetic process model results are used since the adhesive bonding process model is under development. Direct mapping exercises show that the equivalent nonmechanical strain is mapped consistently across dissimilar meshes and that residual stresses, strains, and deformations can be initialized accurately in a structural model using the mapping procedure. Functional mapping exercises with synthetic input data verify the implementation behaves as expected. In one example, the significance of bondline thickness is examined by using a bondline thickness prediction from a process model and a bondline thickness functional map based on new test data. The results indicate that up to a 20% variation in toughness over 40 mm of crack propagation and that the trend of the R-curve (rising or falling) depends on the location of the Teflon insert with respect to the panel. Further work is needed to validate process model and mapping framework.

ACKNOWLEDGEMENTS

The authors wish to acknowledge the support of the NASA Transformational Tools and Technologies (TTT) project. We are also grateful for the technical discussions with Alireza Forghani at Convergent Manufacturing Technologies. Many thanks are due to Tyler Hudson and Kylan Zhao for panel manufacturing, and to Frank Leone for creating python scripts to automate generation of DCB models.

REFERENCES

[1] S. P. Engelstad and S. B. Clay. 2017. "Comparison of Composite Damage Growth Tools for Static Behavior of Notched Composite Laminates," *Journal of Composite Materials,* vol. 51, no. 10, pp. 1493-1524.

[2] J. Action, F. A. Leone and N. V. D. Carvalho. 2020. "Progressive Damage Analysis of a Multi-Stringer Post-Buckled Panel," in *AIAA Scitech 2020 Forum*, Orlando, FL.

[3] J. Finlay, A. M. Waas, P. Davidson, J. D. Bartley-Cho and N. Muraliraj. 2023. "Progressive Failure Modeling of Z-Pin Reinforced Composite Pi Joints," in *AIAA SCITECH 2023 Forum*, National Harbor, MD.

[4] S. P. Engelstad, R. W. Koon, J. Action, J. M. Riga, A. M. Waas, D. Robbins, R. W. Dalgarno, A. R. Arafath and A. Poursartip. 2015. "Integrated Computational Materials Engineering for Airframe Composite Structure Applications," in *56th AIAA/ASCE/AHS/ASC Structures, Structural Dynamics, and Materials Conference*, Kissimmee, FL.

[5] R. Larson, A. Bergan, F. Leone and O. G. Kravchenko. 2023. "Influence of Stochastic Adhesive Porosity and Material Variability on Failure Behavior of Adhesively Bonded Composite Sandwich Joints," *Composite Structures,* vol. 306, p. 116608.

[6] R. S. Kumar. 2021. "Effects of Randomly Distributed Defects on Mode-I Interlaminar Fracture of Composite Materials," *Engineering Fracture Mechanics,* vol. 248, p. 107699.

[7] R. S. Kumar. 2021. "Mode-II Interlaminar Fracture of Composite Materials in the Presence of Randomly Distributed Defects," *International Journal of Fracture,* vol. 231, no. 2, p. 201–221.

[8] Lockheed Martin Corporation. 2018. "Integrated Computational Methods for Composite Materials (ICM2)," Marietta, GA.

[9] Convergent Manufacturing Technologies. April 2023. *COMPRO Users' Guide v.1.1*.

[10] N. Mayer, B. Van Den Broucke, J. Prowe, T. Havar and R. Hinterhölzl. 2016. "Finite Element Mapping for Incompatible FE Meshes of Composite Structures," *Advances in Engineering Software,* vol. 99, pp. 81-88.

[11] T. H. Cormen, C. E. Leiserson, R. L. Rivest and C. Stein. 2022. *Introduction to Algorithms*, Fourth Edition, Cambridge, MA: The MIT Press.

[12] S. Wanthal, J. D. Schaefer, B. Justusson, I. Hyder, S. Engelstad and C. Rose. 2017. "Verification and Validation Process for Progressive Damage and Failure Analysis Methods in the NASA Advanced Composites Consortium," in *American Society for Composites 32nd Technical Conference*, West Lafayette, IN.

[13] A. J. Kinloch and S. J. Shaw. 1981. "The Fracture Resistance of a Toughened Epoxy Adhesive," *The Journal of Adhesion,* vol. 12, pp. 59-77.

[14] V. Tvergaard and J. W. Hutchinson. 1996. "On the Toughness of Ductile Adhesive Joints," *Journal of the Mechanics and Physics of Solids,* vol. 44, no. 5, pp. 789-800.

[15] P. Virtanen, R. Gommers, T. E. Oliphant, et al. 2020. "SciPy 1.0: Fundamental Algorithms for Scientific Computing in Python," *Nature Methods,* vol. 17, no. 3, pp. 261-272.

[16] N. V. De Carvalho, M. W. Czabaj and J. G. Ratcliffe. 2021. "Piecewise-Linear Generalizable Cohesive Element Approach for Simulating Mixed-Mode Delamination," *Engineering Fracture Mechanics,* vol. 242, p. 107484.

[17] Dassault Systèmes Simulia Corporation. 2021. *Abaqus Online Documentation: Version 2021.*

[18] A. J. Paris and P. C. Paris. 1981. "Instantaneous Evaluation of J and C," *International Journal of Fracture,* vol. 38, pp. R19-R21.

[19] Solvay, "FM 209-1," [Online]. Available: https://www.solvay.com/en/product/fm-209-1. [Accessed 2023].

[20] Dassault Systèmes Simulia Corporation. 2018. *Abaqus Online Documentation: Version 2018.*

[21] ASTM Standard D5528/D5528M-21. 2021. *Standard Test Method for Mode I Interlaminar Fracture Toughness of Unidirectional Fiber-Reinforced Polymer Matrix Composites,* West Conshohocken, PA: ASTM International.